Aerodynamic Stability and Performance of Next-Generation Parachutes for Mars Descent

Author:
Keir Gonyea

Advisor:
Dr. Robert D. Braun

July 18, 2013

Aerodynamic Stability and Performance of Next-Generation Parachutes for Mars Descent

Keir C. Gonyea[1]
Georgia Institute of Technology, Atlanta, GA, 30332

Christopher L. Tanner[2] and Ian G. Clark[3]
Jet Propulsion Laboratory, California Institute of Technology, Pasadena, CA, 91109

Laura K. Kushner[4] and Edward T. Schairer[5]
NASA Ames Research Center, Moffett Field, CA 94035

Robert D. Braun[6]
Georgia Institute of Technology, Atlanta, GA, 30332

The aerodynamic stability and performance characteristics of next-generation supersonic parachutes were determined through wind tunnel testing. Canopy configurations included the disk-gap-band (DGB), ringsail, and ringsail-variant designs referred to as the disksail and starsail. Stereo photogrammetric processing was performed during testing, which was then used to estimate the static and dynamic moment coefficient curves as a function of total angle of attack. The dynamic components of the angle of attack and sideslip angle were shown to be significant, heavily influencing the resulting total angle of attack profile and moment coefficients. Uncertainty in the apparent mass of the canopies resulted in uncertainty in the moment coefficient magnitudes. From the stability curves, the peak moment, trim total angle of attack, and pitch stiffness at the trim angle could be determined. Parachute stability was assessed in the context of drag load and geometric porosity. An inverse relationship between the drag load and the stability of the canopies was generally seen. The DGB canopies tended to be more stable while the ringsail and disksail canopies had more drag. Similar stability properties as the DGB with slightly higher drag loads were obtained by increasing the geometric porosity distribution around the crown of the disksail canopies.

_____

[1] Graduate Research Assistant, School of Aerospace Engineering, keir@gatech.edu, AIAA student member
[2] Lead Test Engineer, christopher.l.tanner@jpl.nasa.gov, AIAA member
[3] LDSD Principal Investigator, ian.g.clark@jpl.nasa.gov, AIAA member
[4] Research Engineer, ACI/Experimental Aero-Physics Branch, laura.k.kushner@nasa.gov
[5] Aerospace Engineer, Experimental Aero-Physics Branch, edward.t.schairer@nasa.gov
[6] David and Andrew Lewis Professor of Space Technology, School of Aerospace Engineering, robert.braun@aerospace.gatech.edu, AIAA Fellow

Nomenclature

C_m	static moment coefficient
C_{m_0}	local intercept of static moment curve
C_{m_α}	local slope of static moment curve
$C_{m_{\dot{\alpha}}}$	dynamic moment coefficient
C_T	tangential force coefficient
D_0	parachute reference diameter
D_p	parachute projected diameter
g	acceleration due to gravity
k_{44}	apparent inertia coefficient
m	mass of the parachute canopy
M_{aero}	moment due to canopy aerodynamics
Q_w	local dynamic pressure at the canopy
R_{cm}	distance from the ball joint to the canopy center of mass
R_{cp}	distance from the ball joint to the canopy center of pressure
R_v	distance from the ball joint to the canopy vent
S_0	parachute reference area
V_c	wind velocity at the canopy
V_w	wind velocity at the canopy corrected for canopy rotation
V_t	velocity of the canopy tangent to its arc of motion
x, y, z	wind tunnel frame coordinates (x streamwise, y lateral, z vertical)
α	angle of attack
α_G	total geometric angle
α_T	total angle of attack
β	sideslip angle
$\Delta\alpha, \Delta\beta$	dynamic contribution to the angle of attack and sideslip angle, respectively
γ	geometric angle between V_c and V_t
ϕ	clock angle (angle from vertical of wind tunnel axis projected onto yz-plane, positive clockwise)
ρ_∞	freestream air density
θ, ψ	geometric pitch and yaw angles, respectively
Ω	magnitude of the angular velocity of the canopy

Subscripts

v	location of the canopy vent
θ	motion in the pitch plane
ψ	motion in the yaw plane
trim	trim total angle of attack

Superscripts

’	parachute body axes

Acronyms

BLDT	balloon launched decelerator test program
CFD	computational fluid dynamics
DGB	disk-gap-band
DS	disksail
LDSD	low density supersonic decelerator
MSL	mars science laboratory
MER	mars exploration rover
NFAC	national full-scale aerodynamics complex
PEPP	planetary entry program
PIA	parachute industry association
RMS	root mean square
RS	ringsail

SHAPE	supersonic high-altitude parachute experiment
SPED	supersonic planetary entry decelerator program
SPTT	subsonic parachute technology task
SS	starsail
TDT	transonic dynamics tunnel

I. Introduction

Parachutes designed to decelerate robotic payloads at Mars experience the unique combination of high Mach number and low-density inflation conditions.[1] The first parachute tests conducted at conditions pertinent to Mars entry were wind tunnel tests performed by J. D. Maynard, who tested both rigid and flexible parachute models at supersonic, high earth-altitude conditions similar to those achieved during Mars entry.[2] Many important results were observed from these tests including the effects of Mach number and canopy porosity on the aerodynamic stability and drag of the parachute. Later wind tunnel tests conducted at NASA confirmed and expanded these results.[3,4]

After the early wind tunnel tests, NASA conducted a series of supersonic, high-altitude flight tests in the 1960's and 1970's called the Planetary Entry Program (PEPP), Supersonic Planetary Entry Decelerator Program (SPED), and the Supersonic High-Altitude Parachute Experiment (SHAPE). These tests were designed to increase the capabilities of supersonic parachutes and provide the foundation for future missions to Mars. High altitude tests involved either lofting the parachute and payload to high altitudes via a balloon and then accelerating the system to the test velocity using rockets or launching the system on a sounding rocket and deploying the parachute at the desired altitude and velocity.[5,6] A total of sixteen such tests were performed on disk-gap-band (DGB), ringsail, and cross parachutes between Mach numbers of 1.1 and 3.3 and dynamic pressures of 5.9 and 20.3 pounds per square foot.[7-21] These tests provided important information about drag, stability, and inflation characteristics versus Mach number for parachutes in Mars flight-relevant conditions.[22-25]

Subsequent parachute testing for Mars applications was primarily conducted to qualify the parachute decelerator systems of upcoming Mars landers. The largest of these was during the development of the DGB parachute decelerator for the Viking mission in 1975. The Viking parachute qualification test program involved wind tunnel testing as well as low-altitude drop tests and high-altitude flight tests to establish the parachute drag and stability performance, loading, and inflation characteristics. A nominal drag curve was obtained from subscale wind tunnel testing conducted at four different facilities at Mach numbers between 0.2 and 2.6.[26] Following the wind tunnel testing, a series of subsonic, low-altitude drop tests were performed to test the parachute system configuration and loading performance.[27] The drop tests involved dropping the parachute (attached to a slender forebody) from an aircraft at 50,000 feet. The final qualification steps, known as the Balloon Launched Decelerator Test program (BLDT), included four high-altitude flight tests similar to those from the PEPP, SPED, and SHAPE programs to evaluate the parachute inflation, drag, and stability characteristics behind the Viking aeroshell.[28] The BLDT test program successfully demonstrated both subsonic and supersonic performance of the Viking DGB in a low-density environment similar to Mars flight conditions as well as provided a fundamental dataset for future parachute qualification since further flight testing proved to be prohibitively expensive.

After the Viking parachute development program, parachute testing in support of Mars exploration was suspended for 20 years until the qualification of the Mars Pathfinder canopy. Due to scheduling constraints and the design philosophy of 'better, faster, cheaper,' the Mars Pathfinder team did not conduct high-altitude flight tests or wind tunnel tests of the parachute system.[29] Instead, parachute development relied heavily on the Viking test results and full-scale, low-altitude flight tests. Most aspects of the Pathfinder parachute were qualified through similarity to the Viking design. However, the airbag landing system used for terminal descent required higher stability performance than achievable from the Viking canopy. The additional flight tests were performed to validate the requisite modifications to the Phoenix canopy.

The next series of Mars parachute tests were conducted prior to the Mars Exploration Rover (MER) mission. The MER parachute test campaign was much more involved than that of the Pathfinder mission, including subscale and full-scale wind tunnel tests and low-altitude drop tests.[30] However, the MER parachute development still made ample use of Viking heritage to avoid the costs of expensive high-altitude flight testing. In addition to the low-altitude drop tests, structural qualification of the parachute was achieved through full-scale wind tunnel testing at the NASA Ames National Full-Scale Aerodynamics Complex (NFAC) 80-by-120-foot test section, which provided greater control over the test conditions.[31-34] Of particular interest to the current investigation were the subscale wind tunnel tests in the NASA Transonic Dynamics Tunnel (TDT), performed to asses the aerodynamics and drag of various DGB canopies.[35] In general, experimental determination of parachute aerodynamics is difficult because they

are highly flexibly structures, have complex flow interactions, and exhibit apparent mass effects. The MER subscale wind tunnel testing was able to characterize some these effects by holding a textile parachute at the vent and rotating the parachute-payload system through a range of angles of attack. This testing was thus able to resolve parachute aerodynamic and drag curves (C_M, C_N, and C_T) as functions of angle of attack. These curves have since served as the basis dataset for Mars parachute modeling for all subsequent US missions.

In 2004, JPL performed the first parachute technology development program since the PEPP, SPED and SHAPE supersonic flight tests.[36] The Subsonic Parachute Technology Task (SPTT) conducted four high-altitude balloon drop tests to qualify a subsonic ringsail parachute for future Mars missions.[37,38] The SPTT parachute was designed to be a subsonic main canopy, deployed by the supersonic Viking canopy. Therefore, balloon drop tests were not required to accelerate the parachute supersonically, which greatly reduced the test program costs. Unfortunately, due to reefing and balloon malfunctions, none of the tests were successful and the second-stage ringsail parachute was not used on subsequent missions.

Parachute testing for the Phoenix Mars Scout mission was less intensive since it was able to land using the Viking canopy.[39] Ground testing and low-altitude drop testing were conducted for qualification of the parachute but wind-tunnel and flight tests were not required since the heritage Viking data applied directly to this canopy.

The most recent mission to Mars, Mars Science Laboratory (MSL), is reaching the boundary of what can be landed using the Viking heritage technology. As a result, qualification of the MSL DGB involved a number of different wind tunnel tests as well as validation using Computational Fluid Dynamics (CFD).[40] Full-scale and subscale wind tunnel testing was performed to validate the strength, drag and stability of the canopy while Viking heritage test results were used to qualify the canopy inflation and supersonic performance since high-altitude flight tests were infeasible.[41,42] In addition, to supplement these datasets, supersonic wind tunnel testing of rigid and flexible subscale models was conducted along with CFD simulations to predict the MSL canopy supersonic performance.[43-48]

The current investigation is part of the Low Density Supersonic Decelerator (LDSD) project, developing a next-generation supersonic parachute to be considered for use on future Mars missions.[49] Subscale wind tunnel testing is being performed to estimate the aerodynamic and drag curves of various supersonic canopy designs. Due to the large parachute diameter, rocket sled testing will be used to assess the canopy strength. Finally, supersonic-flight tests similar to those performed during the pre-Viking development programs will be conducted, where the parachute system is flown on a balloon and then accelerated to the supersonic inflation conditions by a rocket motor. These tests will broaden the heritage data sets, particularly the supersonic flight test data, and allow for the continued development of heavier, more advanced robotic missions to Mars.

II. Approach and Test Setup

A. Approach

A second portion of the MER TDT test involved using a free flying parachute to determine drag performance.[35] Schoenenberger et al. used video data from a downstream camera to extract the parachute stability coefficients.[50] By tracking the location of the canopy vent in each video frame and transforming those data into a two-dimensional position in space, the total angle of attack and its first and second derivatives could be computed. These values were subsequently used in a parameter estimation methodology to calculate the static and dynamic aerodynamic coefficients at a given total angle of attack. The aerodynamics calculated for the parachute correlated well with the static test results for the same canopy.[35] This parameter estimation methodology, outlined in Ref. 50, is well suited to large-scale parachute testing and is the primary method used herein to resolve the parachute stability characteristics.

Since conversion of video data into parachute aerodynamics was not a primary objective of the TDT experiment, several approximations had to be made in order to compensate for the lack of some pieces of data. In particular, the use of a single downstream video camera caused ambiguity in the parachute location and the rapid motion of the canopy relative to the video frame rate induced error in the calculation of the angular rates and accelerations. The full-scale testing that formed the basis for the present investigation attempted to increase the knowledge of the parachute position by utilizing stereo photogrammetry and improve the calculation of angular derivatives by acquiring data at 60 Hz.

B. Canopy Description

A total of 4 different canopy types and a total of 13 different configurations were tested.[51] Canopies flown were sub-scale (approximately 35% diameter of canopies to be flight tested) with representative gore and ring structures. All test articles had a nominal diameter (D_0) of 11.8 m (38.8 ft) and a suspension line length of $1.7D_0$. The majority

of the canopies were constructed from PIA-C-44378 "F-111" nylon broadcloth, which has a fabric permeability of less than 5 $ft^3/min/ft^2$. For the canopies constructed from F-111 nylon, the total porosity is set equal to the geometric porosity since the contribution from fabric porosity is assumed to be negligible.

Two main parameters were varied in the test articles: the magnitude of the geometric porosity and the distribution of the geometric porosity. Generally, higher drag canopies tend to be less stable; thus any improvement in stability from an increase in geometric porosity is expected to be coupled with a reduction in drag. However, it is hypothesized that intelligent modifications to the geometric porosity distribution can balance the increase in stability with a minimal reduction in drag. To accomplish this goal, sail panels were removed from rings located at various distances from the canopy skirt to determine if it was advantageous to preference the geometric porosity distribution near or away from the skirt. In addition, different circumferential porosity distributions were investigated by removing either a full ring or every other panel. (Note that for the ringsail variants, higher number rings are located further away from the canopy apex, or closer to the canopy skirt). The following designs were tested:

1) Disk-gap-band: DGB canopies are constructed by separating a flat circular disk and a cylindrical band of fabric by an open gap. The DGB canopy serves as the reference by which the next-generation parachutes are assessed. Two configurations were tested:
   a. DGB-1: a flight spare of the parachute used for the Mars Phoenix Scout lander mission, constructed using MIL-C-7020 Type I nylon, which has a permeability of approximately 100 $ft^3/min/ft^2$. For this canopy, the contribution from fabric porosity is non-negligible and the total porosity was calculated to be between 12-18%.
   b. DGB-2: a replica of the Phoenix DGB constructed using F-111 nylon. This test article is shown in Fig. 1a.
2) Ringsail: ringsail parachutes are modifications of ringslot parachutes that add fullness to the fabric panels and allow for more airflow through the canopy. Five configurations were tested:
   a. RS-0: a subscale version of a ringsail parachute tested in the SPTT program.[37] A picture of this test article is shown in Fig. 1b.
   b. RS-1: the RS-0 canopy with two-thirds of ring 19 removed.
   c. RS-2: the RS-0 canopy with 27% of rings 17, 18 and 19 removed.
   d. RS-3: the RS-0 canopy with all of ring 19 removed.
   e. RS-4: the RS-0 canopy with all of rings 18 and 19 removed.
3) Disksail: the disksail canopy is a modification of the Ringsail canopy that replaces the first ten rings around the canopy vent with a flat circular disk. The goal of this configuration was to decrease geometric porosity in the crown of the parachute to increase drag and allow that porosity to be redistributed to other portions of the canopy. Five configurations were tested:
   a. DS-1: the disksail as described above and as shown in Fig 1c.
   b. DS-2: the DS-1 canopy with half of ring 11 removed.
   c. DS-3: the DS-1 canopy with all of ring 11 removed.
   d. DS-4: the DS-1 canopy with all of ring 11 and half of ring 17 removed.
   e. DS-5: the DS-1 canopy with all of ring 11 and half of rings 17 and 18 removed.
4) Starsail: the starsail canopy is a modification of the Ringsail where multiple gores are replaced with a solid material creating a star pattern. The goal of this configuration is to change how the geometric porosity is distributed throughout the canopy to retain drag and obtain desirable stability characteristics. Portions of rings 17-20 were removed to obtain a geometric porosity approximately equal to the DGB. One starsail configuration was tested and is shown in Fig. 1d.
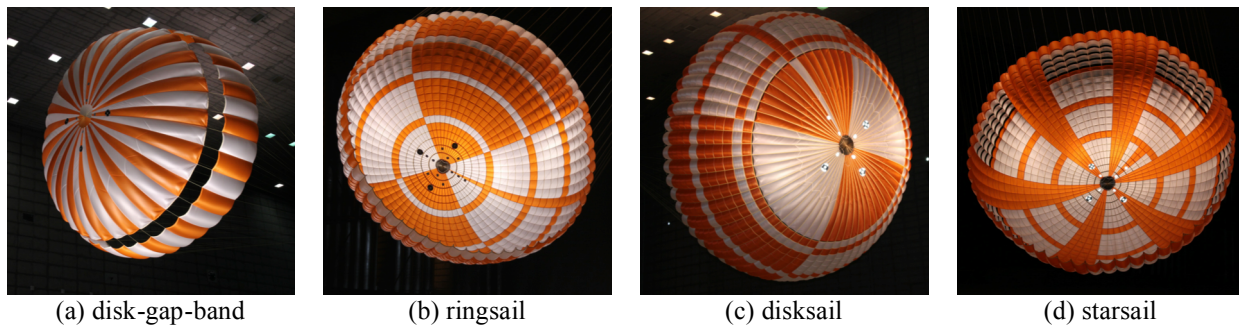

| (a) disk-gap-band | (b) ringsail | (c) disksail | (d) starsail |

Figure 1. Primary canopy configurations used in NFAC testing.

Each canopy was equipped with fourteen retro-reflective targets on both sides of the canopy that appeared in high contrast against the test article and allowed for the canopy to be tracked by the photogrammetry system described in Section II.C. Fiducial target material was carefully selected to maximize light return across a relatively broad range of incidence angles. Targets were located in three concentric rings around the vent with coded target patterns on the outer-most ring to resolve parachute roll about its axis of symmetry. The target pattern is shown in Fig. 2.

Figure 2. Retro-reflective target pattern on each test article.

C. Test Conditions

Wind tunnel testing was performed at the National Full-scale Aerodynamics Complex 80- by 120-foot (80x120) Wind Tunnel at the NASA Ames Research Center. Parachutes were fixed to a strut at the center of the test section via a load arm and ball joint. Mounted to the front of the strut was an aeroshell simulator, intended to approximate the wake generated by the forebody that will be present during flight. This aeroshell simulator was fixed to the strut and was not allowed to move with the parachute. A diagram of the test setup can be seen in Fig. 3.
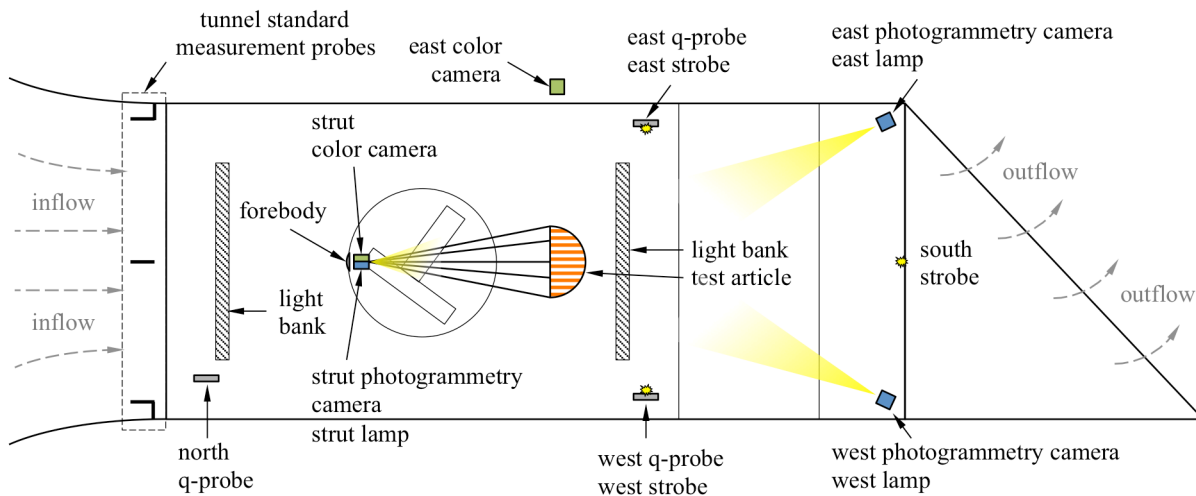

Figure 3. Planview of the wind tunnel test section.

The canopies were tested at nominal freestream wind velocities of approximately 15 and 25 kts, which were dictated primarily by the NFAC operating conditions. Since testing was conducted at sea level density, the dynamic pressures were approximately 0.8 and 2.5 psf, respectively. These values are lower than typical parachute operating dynamic pressures at Mars (7.3 to 15.7 psf), which was acceptable since this test was designed to determine relative stability and drag performance between canopies, not loading capabilities. Pressure probes measured the dynamic pressure during the test and were located both upstream of the strut to measure the freestream conditions and downstream of the canopy skirt to measure blockage effects.

D. Photogrammetry System

1. Photogrammetry Setup

The purpose of the photogrammetry system was to accurately measure the position of the test articles in three-dimensional space such that their static and dynamic stability characteristics could be estimated. The photogrammetry hardware consisted of three high-resolution (2352x1728 pixels) synchronized cameras, two downstream of the parachute on the floor of the test section diffuser and one upstream of the parachute mounted on the strut just below tunnel centerline. The locations of the cameras and the choice of lenses were determined using virtual-imaging software to predict the camera views and ensure that the canopies would be visible over the expected range of positions.[52] The two downstream cameras were placed symmetrically near the corners of the test section to provide stereo imaging of the outer surface of the canopy. They were located sufficiently far downstream to be able to view the retro-reflective targets on the canopy at up to 20° total angle of attack in any direction. The upstream camera was mounted just below the riser attachment and provided a full view of the inside surface of the canopy. The cameras acquired images at 60 Hz – more than ten times the oscillation frequency of the parachute,

thereby eliminating any aliasing of the canopy motion. High-intensity lamps were placed next to each camera to maximize the light output of the retro-reflective targets on the canopy and minimize uncertainty in position tracking. The photogrammetry configuration relative to the overall test set-up can be seen in Fig 3. A synchronized view from each of the photogrammetry cameras is shown in Fig. 4.
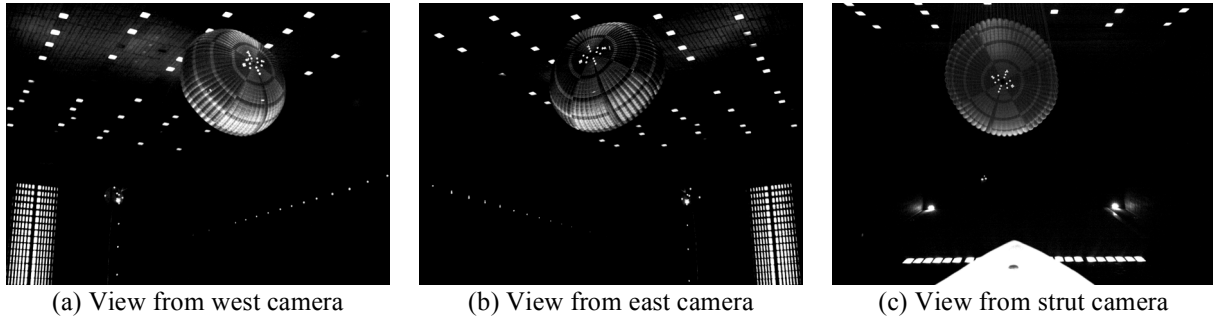

| (a) View from west camera | (b) View from east camera | (c) View from strut camera |

Figure 4. Synchronized images from the three photogrammetry camera views. Stereo photogrammetric measurements were computed using the east and west views.

2. Photogrammetry Calibration

The biggest challenge in making photogrammetry measurements on such a large scale was calibrating the cameras. Two independent calibration methods were used. The first and simplest method was Direct Linear Transformation, which required imaging at least six targets in the region of interest whose spatial coordinates were known.[53] The second method required measuring the "internal orientation" of each camera (focal length, lens distortion corrections, and location of the optical axis in the image plane) before the cameras were mounted. This was accomplished by acquiring images with each camera of a planar array of known targets. These targets were applied in a rectangular grid to one sidewall of the test section. Then, after the cameras were mounted in their final positions and pointed, the spatial positions and point angles of the cameras ("external orientation") were computed from images of a set of targets in the fields of view whose spatial coordinates were known.

Both calibration methods allowed computation of the spatial coordinates of the targets. Unlike the single-camera measurements used in Ref. 50 and previous photogrammetry measurements of parachutes in the 80x120,[54] the stereo imaging method used for this test allowed for accurate three-dimensional tracking of the vent without assuming a constant distance from the canopy to the point of rotation.

3. Photogrammetry Validation

Uncertainty in the photogrammetry system was determined by comparing the camera measurements of verification targets against their known coordinates. Measurements were made with the targets supported on a lift at three different heights and three different lateral locations at the streamwise position of the canopies. The relative error of the photogrammetry measurements was determined by translating and rotating the measured coordinates of the targets to minimize the root mean square (RMS) difference with the true coordinates. The resulting minimum RMS error was less than half of an inch. The uncertainty in the absolute position of the targets was estimated directly by measuring to known reference points. Based on these measurements, the uncertainty in absolute position was less than one inch. These uncertainty estimates are consistent with the expected uncertainty due to a one-pixel error in locating targets in the images. The spatial position of the vent was calculated using both the Direct Linear Transformation and the internal/external calibration methods, resulting in similar coordinates. The internal/external calibration method was ultimately selected to generate all of the data herein.

III. Data Analyses

A. Canopy Vent Coordinates to Geometric Angles

Once the position history of the canopy was determined, the coordinates of the vent were converted into geometric angles, which are more convenient for describing the rotational motion of the parachute. Geometric angles are defined here as angles that are dependent only on the parachute's position with respect to the wind tunnel and do not take into account the parachute's motion with respect to the wind. A diagram showing the wind tunnel and parachute reference frames as well as the relevant geometric angles is shown in Fig. 5. The wind tunnel frame is denoted as $\{x, y, z\}$ and the parachute frame is denoted as $\{x', y', z'\}$ with the origin located at the ball joint, The parachute angular velocity is defined as Ω. The parachute and wind tunnel frames are related by a series of Euler

rotations, first by the pitch angle (θ) about the y-axis, followed by the yaw angle (ψ) about the z'-axis. The full rotation matrix can be seen in Eq. (1).

$$\begin{bmatrix} x \\ y \\ z \end{bmatrix} = \begin{bmatrix} \cos\theta\cos\psi & -\cos\theta\sin\psi & \sin\theta \\ \sin\psi & \cos\psi & 0 \\ -\sin\theta\cos\psi & \sin\theta\sin\psi & \cos\theta \end{bmatrix} \begin{bmatrix} x' \\ y' \\ z' \end{bmatrix} \tag{1}$$

The length of the parachute from the ball joint to the vent is defined as R_v. Knowing R_v and the $\{x_v, y_v, z_v\}$ coordinates of the canopy vent, the pitch and yaw angles can be calculated via Eqs. (3) and (4).

$$R_v = \sqrt{x_v^2 + y_v^2 + z_v^2} \tag{2}$$

$$\theta = \sin^{-1}\left(-\frac{z_v}{R_v\cos\psi}\right) \tag{3}$$
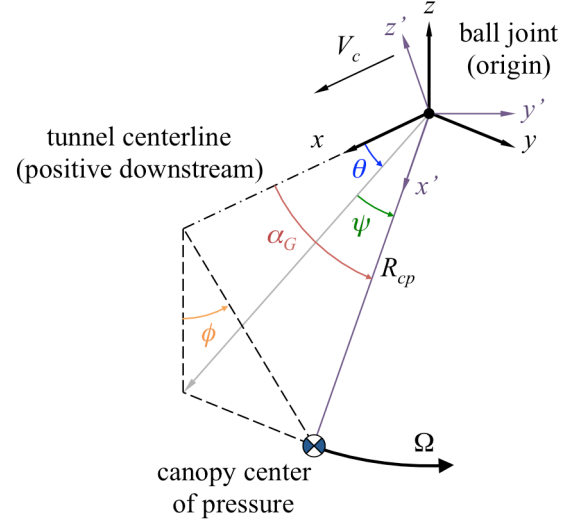
$$\psi = \sin^{-1}\left(\frac{y_v}{R_v}\right) \tag{4}$$

Figure 5. Wind tunnel and canopy coordinate systems.

Two other geometric angles that are useful to define are the total geometric angle (α_G) and clock angle (ϕ). The total geometric angle is the total angular distance between the parachute x'-axis and the wind tunnel x-axis. Note that the total geometric angle is not the same as the total angle of attack, which will be defined later. The clock angle describes the parachute position in the yz-plane when looking upstream. It is defined to be $\phi = 0$ when $y_v = 0$ and $z_v > 0$ and $\phi = \pi/2$ when $z_v = 0$ and $y_v > 0$. The total geometric angle and the clock angle can be calculated via Eqs. (5) and (6).

$$\alpha_G = \cos^{-1}\left(\frac{x_v}{R_v}\right) \tag{5}$$

$$\phi = \tan^{-1}\left(\frac{\sin\theta\cos\psi}{\sin\psi}\right) \tag{6}$$

1. Calculating the Total Angle of Attack and its Derivatives

The total angle of attack can be expressed in terms of the traditional angle of attack and sideslip angle as in Eq. (7). Note that the total angle of attack is always positive.

$$\alpha_T = \cos^{-1}\left[\cos\alpha\cos\beta\right] \tag{7}$$

If the canopy is stationary, then the angle of attack is equal to the pitch angle, the sideslip angle is equal to the yaw angle, and the total angle of attack is equal to the total geometric angle. However, if the parachute is moving, then the rotational motion alters the local wind velocity at the canopy and introduces dynamic contributions ($\Delta\alpha, \Delta\beta$) to the geometric pitch and yaw angles, as in Eqs. (8).

$$\alpha = \theta + \Delta\alpha \tag{8.1}$$
$$\beta = \psi + \Delta\beta \tag{8.2}$$

Calculating the aerodynamic coefficients requires knowledge of the first and second derivatives of the total angle of attack with respect to time, which can be calculated using finite differencing. However, since α_T is always positive, its value can change very rapidly around zero and create non-smooth derivatives. An expression for the

first and second derivatives of the total angle of attack was developed that only requires finite differencing of the Euler angles θ and ψ. These angles have both positive and negative magnitudes and vary smoothly in time, making them well suited for differentiation via finite differencing. The first and second derivatives of the total angle of attack are given in Eqs. (9) and (10). Additional details regarding the calculation $\Delta\alpha$, $\Delta\beta$, and their respective derivatives are given in Appendices A and B.

$$\dot{\alpha}_T = \frac{\dot{\alpha}\sin\alpha\cos\beta + \dot{\beta}\cos\alpha\sin\beta}{\sin\alpha_T} \tag{9}$$

$$\ddot{\alpha}_T = \frac{\ddot{\alpha}\sin\alpha\cos\beta + \ddot{\beta}\cos\alpha\sin\beta + (\dot{\alpha}^2 + \dot{\beta}^2 - \dot{\alpha}_T^2)\cos\alpha_T - 2\dot{\alpha}\dot{\beta}\sin\alpha\sin\beta}{\sin\alpha_T} \tag{10}$$

B. Local Wind Velocity at the Canopy

The total wind velocity at the canopy is the vector sum of the freestream wind velocity ($\mathbf{V}_c$) and the wind velocity tangent to the canopy's arc of motion ($\mathbf{V}_t$). Note that the wind velocity tangent to the canopy's arc of motion is equal and opposite to the tangential velocity of the canopy. Thus, it is subtracted from the $\mathbf{V}_c$ as in Eq. (11.1). The total wind velocity (V_w) is the magnitude (L_2- norm) of the total wind velocity vector ($\mathbf{V}_w$) given in Eq. (11.2).

$$\mathbf{V}_w = \mathbf{V}_c - \mathbf{V}_t \tag{11.1}$$

$$V_w = \sqrt{\left(V_c - \dot{x}_{cp}\right)^2 + \dot{y}_{cp}^2 + \dot{z}_{cp}^2} \tag{11.2}$$

The velocity of the canopy tangent to its arc of motion can be expressed in terms of the Euler angles (see Fig. 5) as in Eq. (12). The canopy velocity is taken at the center of pressure (R_{cp}).

$$\mathbf{V}_t = \begin{bmatrix} \dot{x}_{cp} \\ \dot{y}_{cp} \\ \dot{z}_{cp} \end{bmatrix} = R_{cp} \begin{bmatrix} -\dot{\theta}\sin\theta\cos\psi - \dot{\psi}\cos\theta\sin\psi \\ \dot{\psi}\cos\psi \\ -\dot{\theta}\cos\theta\cos\psi + \dot{\psi}\sin\theta\sin\psi \end{bmatrix} \tag{12}$$

C. Calculating the Aerodynamic Coefficients

The aerodynamic moments on the parachute are represented as a static moment, dependent on the parachute's total angle of attack, and a dynamic moment, dependent on the instantaneous rate of change of the total angle of attack. The static moment coefficient is locally linearized at each total angle of attack into the pitch stiffness coefficient (C_{m_α}) and the moment coefficient at $0°$ total angle of attack (C_{m_0}), as in Eq. (13.1). The resulting expression for the total aerodynamic moment is given in Eq. (13.2).

$$C_m = C_{m_\alpha}\alpha_T + C_{m_0} \tag{13.1}$$

$$M_{aero} = Q_w S_0 D_0 \left[C_{m_\alpha}\frac{D_0}{2V_w}\dot{\alpha}_T + C_{m_\alpha}\alpha_T + C_{m_0} \right] \tag{13.2}$$

The angular behavior with respect to the wind can be used to determine the canopy stability coefficients using parameter estimation.[50] Given that the parachute is an axisymmetric body, the attitude history can be decomposed into motion in two directions - in the same direction as the total angle of attack and in the direction orthogonal to the total angle of attack. For motion in the same direction as the total angle of attack, the rotational equation of motion of the parachute in a wind tunnel can be expressed as in Eq. (14), which accounts for forcing due to aerodynamic moments and gravity. I_{yy} is the moment of inertia of both the canopy and the apparent mass, m is the mass of the canopy only, and g is the gravitational acceleration. Equation (14) can be rearranged to explicitly solve for the aerodynamic moment coefficients as seen in Eq. (15).

$$I_{yy}\ddot{a}_T = Q_w S_0 D_0 \begin{bmatrix} C_{m_{\dot{\alpha}}} & C_{m_{\alpha}} & C_{m_0} \end{bmatrix} \begin{bmatrix} \dot{\alpha}_T \frac{D_0}{2V_w} \\ \alpha_T \\ 1 \end{bmatrix} + mgR_{cp}\begin{bmatrix} \cos\phi\cos\alpha_T \end{bmatrix} \tag{14}$$

$$\begin{bmatrix} C_{m_{\dot{\alpha}}} & C_{m_{\alpha}} & C_{m_0} \end{bmatrix} = \left(\frac{1}{Q_w S_0 D_0}\right)\left(I_{yy}[\ddot{a}_T] - mgR_{cp}[\cos\phi\cos\alpha_T]\right)\begin{bmatrix} \dot{\alpha}_T \frac{D_0}{2V_w} \\ \alpha_T \\ 1 \end{bmatrix}^T \left[\begin{bmatrix} \dot{\alpha}_T \frac{D_0}{2V_w} \\ \alpha_T \\ 1 \end{bmatrix}\begin{bmatrix} \dot{\alpha}_T \frac{D_0}{2V_w} \\ \alpha_T \\ 1 \end{bmatrix}^T\right]^{-1} \tag{15}$$

Equation (15) was simultaneously solved across a small range (or bin) of total angles of attack in order to obtain a set of coefficients that are representative of the parachute behavior within that α_T range. This bin was then incrementally stepped across the full range of α_T data in order to obtain a relatively smooth curve relating the moment coefficients to the total angle of attack. The resultant coefficients represent the average total angle of attack within each bin. The use of a larger bin size will result in a smoother curve, but will tend to bias the coefficients towards those angles of attack that occurred the most. The increment at which the bin is set controls the density of points along the curve. The upper and lower bounds of the moment curves are limited by the angles that were traversed by the parachute during testing and the bin size selected.

D. Discussion of the Apparent Mass

Parachute aerodynamics are often hard to analyze because of complex interactions with the surrounding flowfield. For example, when a parachute is moving in a fluid, any external force that accelerates the parachute must also accelerate the fluid in and around the canopy. This fluid acceleration can be thought of as an additional mass of the system and is often referred to as the apparent mass. The effect of the apparent mass is difficult to isolate since it is dependent on the fluid density, canopy size, canopy porosity, flow compressibility, and flow velocity. The apparent mass is often mathematically described as a 6x6 tensor with values based in both potential flow theory and empirical data.[55]

Ibrahim performed a series of experiments to quantify the apparent inertia of rotating hemispherical, flat circular, guide surface, and ribbon canopies.[56] For each of the canopies, he determined a non-dimensional coefficient of the apparent moment of inertia for rotation around the canopy centroid as well as rotation around the canopy confluence point. The apparent inertia coefficient was non-dimensionalized with respect to a sphere of air of diameter equal to the projected diameter of the canopy as seen in Eq. (16). Apparent inertias ranged from approximately 31% of a full sphere of air for a hemispherical canopy to 9% for a ribbon canopy. Uncertainty in these inertias was not documented.

$$k_{44} = \frac{I_{yy}}{\frac{1}{6}\pi D_p^3 \rho_\infty R_{cm}^2} \tag{16}$$

Given the relatively small weight of the canopies in this test and the high-density air at sea-level, the apparent inertia about the ball joint dominates the I_{yy} term in the present analysis. Since the gravity term in Eq. (15) is much smaller than the aerodynamics term, the moment coefficients are approximately proportional to the apparent inertia. As a result, apparent mass acts as a scaling factor on the calculated moment coefficients. The results of this investigation are provided given the current best estimate of the apparent inertia.

IV. Results

Photogrammetric data was acquired for each canopy, although only a representative set of data are presented herein. For discussion purposes, Figs. 6-8 are presented for the RS-1 canopy at the 25 kt test condition. However, similar trends were also seen for the other canopies and conditions.

A. Two-Dimensional Canopy Motion

Figure 6 shows a two-dimensional trace of the canopy motion in the wind tunnel *yz*-plane (plane perpendicular to the wind tunnel centerline). The dots along the curve represent data at 3 Hz and illustrate that the 60 Hz data rate provided a sufficiently dense sampling of the canopy motion. It can be seen that the parachute stays approximately

within a circle of radius twenty feet, centered near the tunnel centerline. In addition, the parachute covers the entire interior of the circle fairly uniformly. The canopy never develops a circular coning motion near its trim angle of attack. The parachute's time-averaged position in the *y*-direction is negligible, there was no tendency for it to stay on either side of the test section. However, the average position in the *z*-direction is noticeably below zero, which is attributed to gravity acting on the canopy.

Figure 6. Trace of the RS-1 canopy vent.

B. Dynamic Versus Static Angle Contribution

The result of the total angle of attack calculation (described in Section III.A) is displayed in Fig. 7. Figure 7a shows that the wind-relative angles are significantly greater than the geometric angles due to rotation of the canopy. The mean and 95th percentile α_G and α_T are shown in Fig. 7b and indicate that the wind-relative angles can be greater than twice the geometric angles. Figure 7b also shows that the distribution of the angles varies considerably. This is particularly important since the stability curves, which should be calculated based on total angle of attack, would look significantly different if based off of the total geometric angle.

The use of wind-relative angles leads to a non-intuitive relationship between the total geometric angle and the total angle of attack. Figure 8a shows the tangential velocity of the canopy versus the total geometric angle at each point in the parachute trajectory. The tangential velocity is generally high at low total geometric angles and low at high angles. Thus, the parachute momentarily stops rotating when it reaches the maximum total geometric angle and rotates the fastest as it sweeps through the center, similar to simple harmonic motion. This means that the parachute reaches its largest total angle of attack just after passing through the center of the test section (α_G near zero). It then reaches the lowest total angle of attack just after attaining the maximum total geometric angle, while beginning to return to the center of the test section. In other words, the maximum and minimum total geometric angle and the total angle of attack are approximately 180° out of phase from each other. This behavior can be seen in Fig. 8b and is due to the impact of parachute dynamic motion on the local wind velocity.
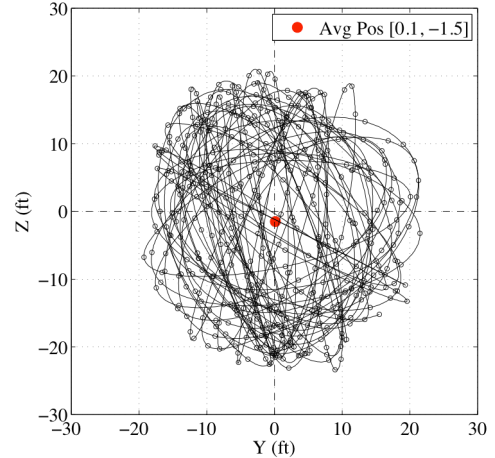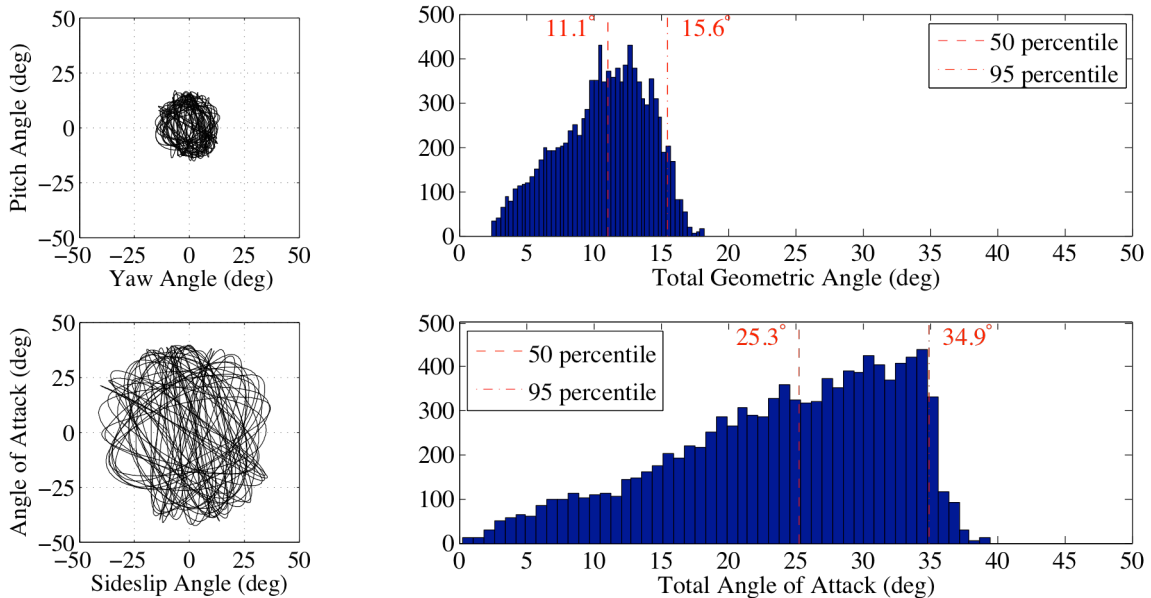

(a) Angular vent trace of the canopy motion over time

(b) Histogram of angles traversed by the parachute

Figure 7. Comparisons of the angular motion of the parachute when using geometric angles and wind-relative angles for the RS-1 canopy.
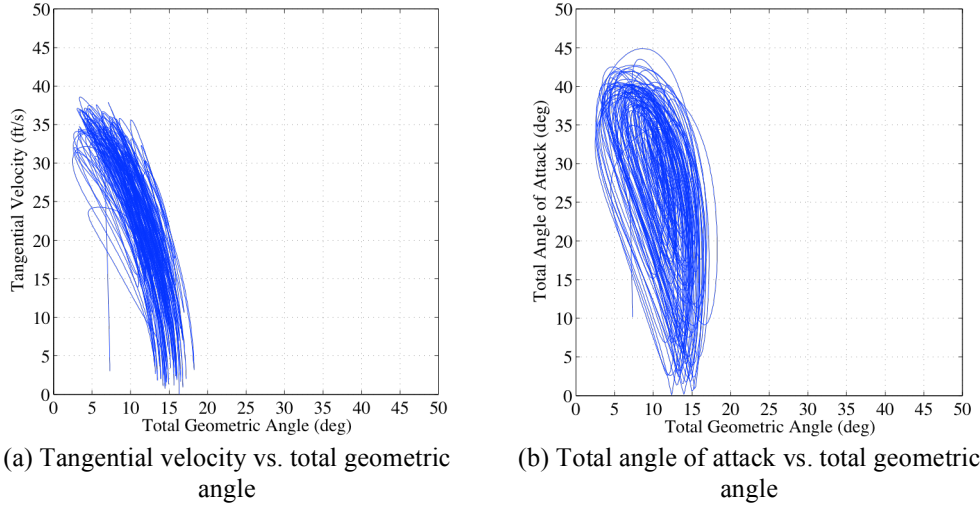
(a) Tangential velocity vs. total geometric angle

(b) Total angle of attack vs. total geometric angle

Figure 8. Comparisons between the tangential velocity and the total angle of attack profiles to the total geometric angle for the RS-1 canopy.

C. Raw Data Reduction and Processing

The stability coefficients were determined using a bin width of 0.5° and a bin step of 0.25°. The bin width was chosen because there were generally over 25 points contained within this bin size, a sufficiently large sample size to generate representative coefficients. The bin step was chosen to provide an adequate number of data points from which to reconstruct a continuous C_m curve. A plot of the resultant C_m data for the RS-1 canopy is shown in Fig. 9 (both the blue circle and purple x symbols). These data were fit using a polynomial that was forced to go through a C_m of zero at 0° total angle of attack (which is typical of axisymmetric bodies). The data appeared to exhibit an unusually high C_m at low total angles of attack, thus some data were excluded from the fit to obtain a reasonable C_m curve, which are seen as the purple x symbols in Fig. 9. These stability estimates are used for the relative comparison of different canopies, although their absolute magnitudes may not be accurate due to the uncertainty in the apparent mass value used in the analysis. This topic is discussed further in Section IV.E.

The trim total angle of attack is the angle where the parachute does not experience an aerodynamic moment (C_m is equal to 0). A low trim angle of attack is desirable since it will be less likely to introduce a destabilizing moment on the payload and because more of the drag force will be oriented along the centerline of the payload. For canopy RS-1, there are two trim angles – 0° and 23° total angle of attack. The positive moment curve slope at 0° is indicative of an unstable trim point, where a small perturbation will force the canopy away from the trim total angle of attack. Conversely, the negative moment curve slope at 23° indicates a stable trim point, where any deviation of the parachute from this point will drive it back to the trim total angle of attack. The magnitude of $C_{m_{\alpha,trim}}$ determines the magnitude of the
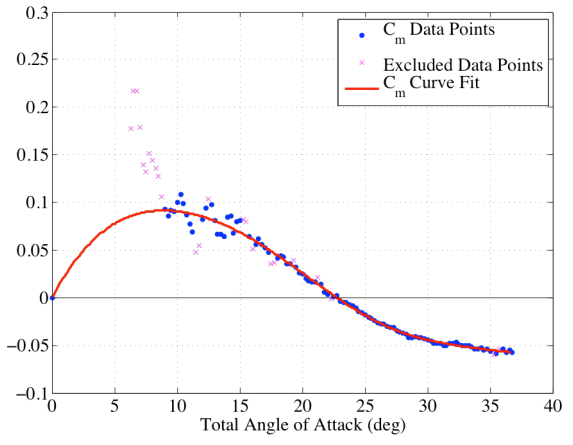

Figure 9. Static moment coefficients and curve fit as a function of the total angle of attack for the RS-1 canopy. X symbols were excluded when performing the curve fit.
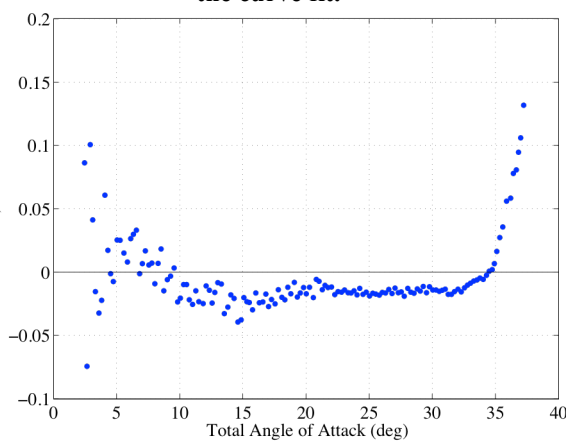

Figure 10. Dynamic moment coefficients as a function of total angle of attack for the RS-1 canopy.

restorative force, or how stable the parachute is at the trim total angle of attack. While a low trim total angle of attack is always considered beneficial, it is not clear what is the best value for $C_{m_{\alpha,trim}}$. If moment curve slope is too low, then the restorative force is relatively weak and the parachute may traverse large angles during descent. However, if the moment curve slope is too large, then the parachute could potentially introduce a violent moment on the payload if it were suddenly displaced from the trim total angle of attack due to a gust of wind or other perturbation. Another important feature of the curve is the peak C_m value. Higher peak values could also cause violent motion and destabilize the system. Therefore, a lower overall C_m curve is considered to be beneficial.

Figure 10 shows a plot of the pitch damping curve for the RS-1 canopy. In this case, the pitch damping coefficient at the trim total angle of attack is less than zero; therefore, the canopy is dynamically stable at this point. However, the curves of different canopies vary widely and there is no overall trend regarding dynamic stability at the trim total angle of attack. To obtain a smooth curve it was necessary to increase the bin size to 1.5°. However, the coefficient values still scatter towards lower total angles of attack. As a result, it is difficult to determine the shape of the pitch damping curve across canopies.

D. Comparison to Prior Wind Tunnel Results

Prior to the Mars Exploration Rover missions, wind tunnel tests of various DGB parachutes were performed in the TDT to determine their drag performance and static stability behavior.[35] Moment values for each canopy were measured by constraining the parachute in a fixture that was rotated through a range of angles of attack. This data serves as a reference for the present DGB tests.

As part of the TDT test campaign, a sub-scale version of the Mars Viking DGB was flown that had a nominal diameter of approximately 5.2 ft and was constructed from MIL-C-7020 Type III nylon. This test was run at sea-level density and a dynamic pressure of 16 psf. This canopy is very similar to the Mars Phoenix Scout canopy (DGB-1) flown in the present NFAC test since the Phoenix DGB gap and band heights were based on the Viking configuration and the fabric permeability of Type I and Type III MIL-C-7020 nylon are similar. The two NFAC DGB-1 tests were conducted at dynamic pressures of 0.8 and 2.5 psf. Figure 11 shows the resulting C_m curves from each of the tests.

Comparison between the TDT and NFAC tests is difficult because the runs were performed at very different dynamic pressures. However, it can be seen that the trim total angle of attack decreases with increasing dynamic pressure, which was similarly observed in TDT testing.[35] Additionally, the peak C_m and the general shape of the C_m curves appear to change with dynamic pressure.

Figure 11. Comparison of C_m curves as a function of total angle of attack for wind tunnel tests performed in the NFAC and the TDT.

E. Apparent Mass Effects

Equation 16 shows that apparent inertia scales with nominal diameter to the fifth power (given that the distance R_{cm} is a function of the nominal diameter). Assuming that the error in the apparent inertia is a constant percentage its nominal value, error in the apparent mass model would be significantly greater for large diameter parachutes than for small parachutes. Uncertainty related to the apparent inertia of the parachute canopies tested at NFAC, as stated in Section III.D, may be one potential cause of the differing C_m curves shown in Fig. 11.

A single apparent inertia coefficient value of 0.05 was used to analyze all of the canopies, despite the fact that they had different geometric porosities and were operating at slightly different dynamic pressures. The dataset in Ref. 56
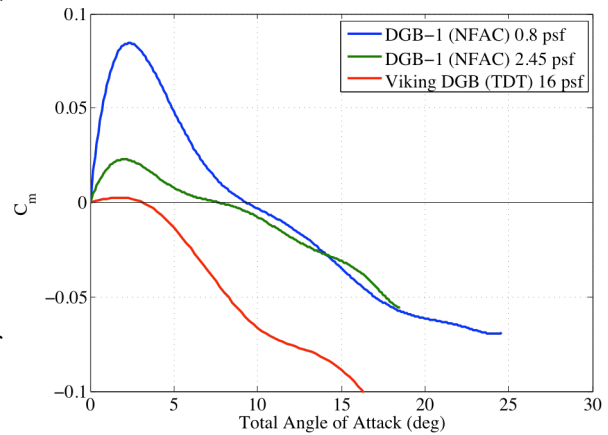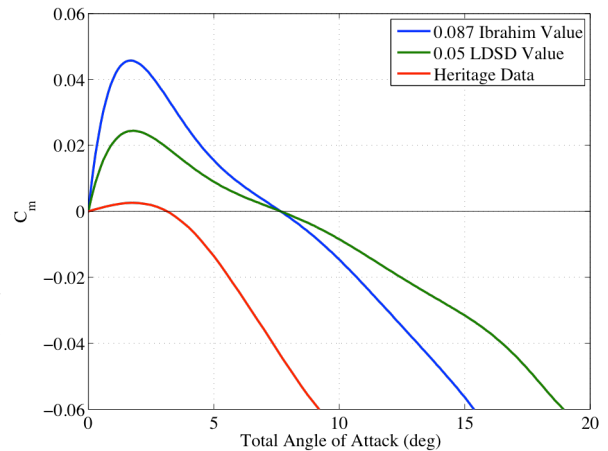

Figure 12. C_m curves calculated using varying apparent inertia coefficients for the DGB-1 canopy compared to heritage data.

does not provide enough data to intelligently select an apparent inertia coefficient that depends on geometric porosity and dynamic pressure. The lowest apparent inertia coefficient cited in Ref. 56 was 0.087, which corresponded to a ringslot canopy with a geometric porosity of approximately 27%. However, this apparent inertia coefficient resulted in a C_m curve that differed significantly from the existing DGB data, as shown in Fig. 12. As such, a value of 0.05 was used, providing a slightly better correlation with the existing DGB data.

F. Comparison Between Canopy Aerodynamics

The stability metrics for each canopy are tabulated in Table 1 along with their averaged tangential force coefficient (C_T) and approximate geometric porosity. Desirable canopies have low trim total angles of attack, static stability ($C_{m_{\alpha,trim}} < 0$), and high averaged tangential force coefficients. (Trim α_T is used here as a metric for stability and average tangential force coefficient is used as a metric for drag since stability and drag information were not directly available). For a next-generation canopy design to have better drag and stability performance than the DGB, the C_M curve should cross 0 at a lower angle, have a lower peak magnitude and have a higher value of averaged C_T.

Table 1. Summary of canopy stability and drag results.

Canopy Number	Canopy Description	Geometric Porosity (%)	Trim α_T (deg)	$C_{m_{\alpha,trim}}$ (1/deg)	Averaged C_T
DGB-1	DGB with high porosity fabric	13	8	-6 x10^{-3}	0.59
DGB-2	DGB with low porosity fabric	13	15	-9 x10^{-3}	0.81
RS-0	Ringsail design tested in 2005	10	23	-6 x10^{-3}	0.99
RS-1	RS-0 without 2/3 ring 19	13	23	-8 x10^{-3}	0.90
RS-2	RS-0 without 27% rings 17, 18, 19	15	24	-7 x10^{-3}	0.91
RS-3	RS-0 without ring 19	16	21	-8 x10^{-3}	0.86
RS-4	RS-0 without rings 18, 19	22	19	-11 x10^{-3}	0.77
DS-0	Disksail as built	9	23	-9 x10^{-3}	1.03
DS-1	DS-0 without 1/2 ring 11	11	19	-8 x10^{-3}	0.98
DS-2	DS-0 without ring 11	13	13	-15 x10^{-3}	0.92
DS-3	DS-0 without ring 11, 1/2 ring 17	16	12	-13 x10^{-3}	0.86
DS-4	DS-0 without ring 11, 1/2 rings 17, 18	19	14	-10 x10^{-3}	0.82
SS	Starsail as built	13	23	-5 x10^{-3}	0.83

1. Disk-gap-band Comparison

Figure 13 shows the static stability curves for the DGB-1 and DGB-2 canopies at the same dynamic pressure. While both canopies have the same geometric porosity, the DGB-1 has a higher total porosity (15-18%) than DGB-2 due to higher fabric permeability. Figure 13 indicates that, for the two DGB parachutes tested, higher fabric permeability effectively decreases the peak C_m value, the trim α_T, and the tangential force. The TDT test was conducted with DGB's having two different material permeabilities as well and trim α_T was similarly observed to decrease.[35] Since DGB parachutes have displayed acceptable stability behavior during prior U.S. Mars missions, the overall performance of each parachute can be determined in relation to the performance of the DGB (for example, equivalent stability with enhanced drag).
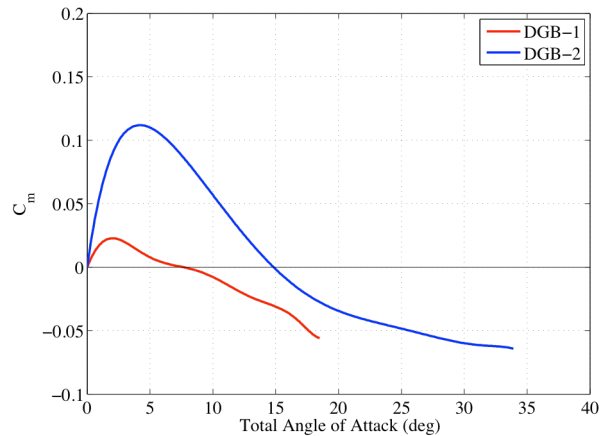

Figure 13. Comparison of C_m curves for the DGB canopies.

2. As-built Canopy Comparisons

Figure 14 shows a comparison of the moment coefficient curves for the F-111 DGB and the as-built ringsail, disksail, and starsail canopies. The DS-0 and RS-0 canopies have similar C_m profiles and similar trim total angles of attack, but the disksail exhibits slightly better drag performance than the ringsail. In fact, Table 1 indicates that other disksail canopies have a smaller trim α_T and equivalent or greater tangential force than ringsail configurations with

similar geometric porosities. Additionally, the C_m curves for disksail canopies tend to have a steeper slope around the trim total angle of attack than for ringsails with equivalent geometric porosities. It is unclear why this trend occurs, but it was evident during testing that the disksail took a slightly more blunt shape than the ringsail, possible due to the presence of the flat disk in the crown.

The starsail canopy has a similar trim total angle of attack to the RS-0 and DS-0 but has less tangential force. The starsail C_m curve is lower than the RS-0 and DS-0 C_m curves and has a relatively shallow slope at the trim total angle of attack, making it nearly neutrally stable. However, given that the disksail and ringsail canopies had the same trim total angle of attack and much higher drag, the starsail is considered to be a less effective design. It should also be noted that the unconventional design of the starsail would have made it more difficult to manufacture than the other two configurations. Therefore, the starsail experiment was not pursued further than the one configuration.
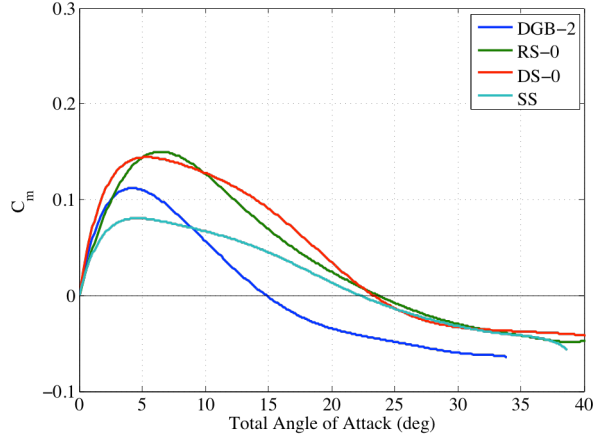

Figure 14. Comparison of the C_m curves for the unmodified canopies.

3. Ringsail Comparisons

The RS-1 and RS-2 canopies were designed to have similar geometric porosity, but with different geometric porosity distributions. The RS-1 canopy concentrated the geometric porosity all to ring 19, where it was hoped that a strong circumferential jet of air flowing out from the canopy would create uniform flow disruption and increase stability (similar to the design of a DGB). The RS-2 canopy distributed the porosity evenly between rings 17, 18, and 19, where it was hoped that the distributed porosity would induce different sized vortices and increase stability. However, manufacturing tolerances and a rushed fabrication schedule resulted in the RS-1 and RS-2 canopies having different geometric porosities. In general, the stability of the RS-0, RS-1, and RS-2 are similar, although the peak value of the C_m curve is slightly different for the each canopy, as shown in Fig. 15a. In addition, the RS-1 and RS-2 canopies produced similar tangential force coefficients, which was approximately 10% lower than the RS-0 canopy. Therefore, the change in the geometric porosity distribution around the shoulder region of the canopy had a relatively minimal effect.
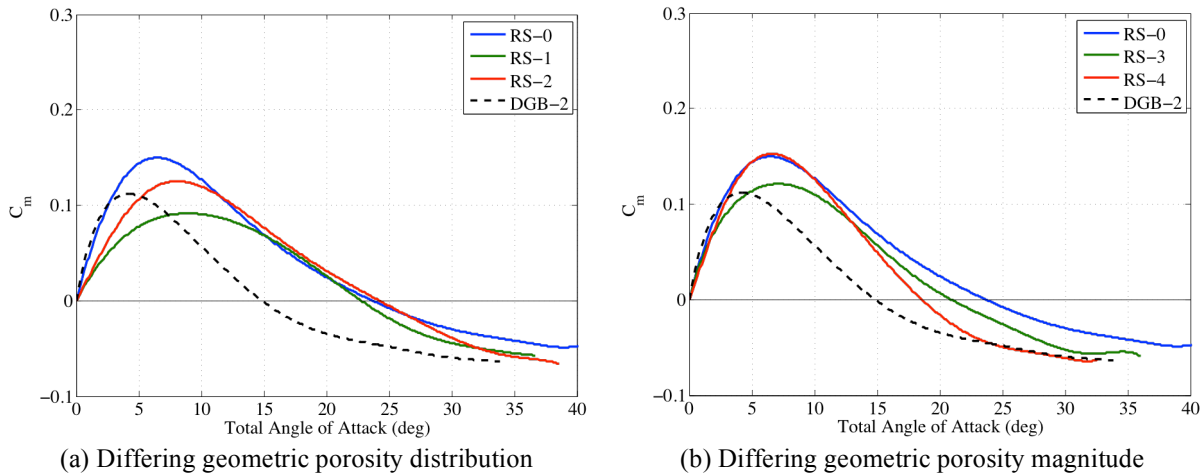

(a) Differing geometric porosity distribution

(b) Differing geometric porosity magnitude

Figure 15. Comparison of C_m curves for the Ringsail canopy modifications.

The magnitude of the geometric porosity was intentionally modified in the RS-3 and RS-4 configurations, increasing the geometric porosity of the RS-0 canopy by approximately 60% and 120%, respectively. All of the porosity was created in the shoulder of the parachute to determine if a larger gap would improve the stability more than in the RS-1 and RS-2 configurations. Figure 15b shows that these changes in the geometric porosity did have a noticeable effect and decreased the trim total angle of attack by 9% and 17% for RS-3 and RS-4, respectively. However, the RS-3 and RS-4 canopies also exhibited a 13% and 22% decrease in the average tangential force

coefficient relative to the RS-0 canopy. In addition, neither RS-3 nor RS-4 exhibited improved tangential force and stability behavior relative to DGB-2.

4. Disksail Comparisons

All of the alternate disksail configurations were obtained by successively removing sail panels from the DS-0 canopy. As seen in Fig. 16a, the first two modifications (DS-1 and DS-2) have the smallest increase in total porosity, but cause the highest reductions in the trim total angle of attack relative to DS-0. Furthermore, configuration DS-2 exhibits a similar trim total angle of attack to the DGB-2 but has a significantly higher tangential force coefficient and a slightly steeper C_m curve at the trim α_T. Further increases in the geometric porosity near the shoulder of the disksail in configurations DS-3 and DS-4 decrease the tangential force but do not significantly alter the trim behavior from the DS-2 configuration, as seen in Fig. 16b. From these data, increasing porosity near the crown of the disksail (as in DS-1 and DS-2) causes the greatest decrease in the trim total angle of attack for the corresponding decrease in the tangential force.
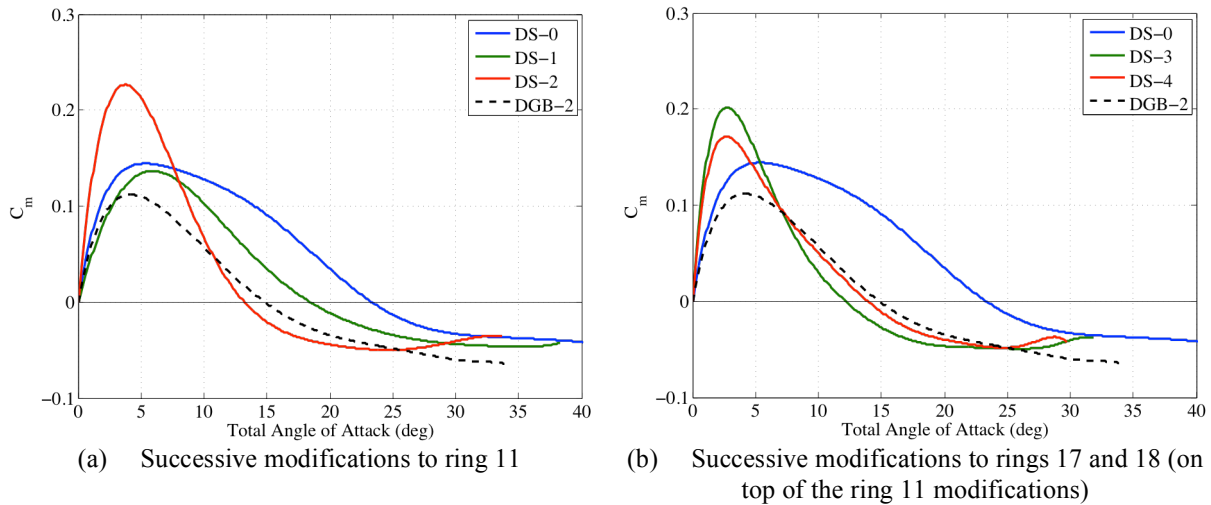

(a) Successive modifications to ring 11

(b) Successive modifications to rings 17 and 18 (on top of the ring 11 modifications)

Figure 16. Comparison of C_m curves for the Disksail canopy modifications.

V. Conclusion

Wind tunnel testing of a wide range of parachute configurations was performed to identify relative drag and stability behavior of canopies with different geometric porosity magnitudes and distributions. Photogrammetric imaging of the canopies during testing was used to accurately determine the position of the canopy vent in the test section to within one inch of uncertainty.

A parameter estimation methodology was used to extract static and dynamic moment coefficients as a function of total angle of attack. This methodology was especially sensitive to uncertainty in the apparent inertia model. Since it was not possible to measure the apparent inertia of the canopies, the apparent inertia was modeled based on historical work and data correlation. Moment coefficients were statistically estimated at every 0.25° α_T and the data was fit using a polynomial. Some moment coefficients at low total angles of attack, where data was generally sparse, were selectively excluded to obtain a better fit. Stability metrics such as the trim angle of attack and moment slope at the trim angle were determined using these fits to aid in the comparison of the canopy configurations.

Geometric and wind-relative angles were calculated from the photogrammetry data. Due to oscillatory motion of the canopy during testing, dynamic contributions to the aerodynamic angles were important, often dominating the static components. This dynamic correction led to a non-intuitive total angle of attack profile.

The behavior of the ringsail, disksail, and starsail canopies were compared against the DGB. Alteration of the geometric porosity in the shoulder region of the ringsail canopy did not yield tangential loads or stability behavior that were more attractive than that of the DGB. Disksail configurations DS-2 and DS-3, however, exhibited significantly greater tangential force and equivalent stability to the DGB. The starsail did not improve upon the DGB performance.

Results were compared with existing DGB data. The overall shape of the DGB C_m curves was similar and the trend of decreasing trim angle of attack with increasing dynamic pressure was observed independently in both tests.

However, uncertainty in the apparent mass and the effects of scaling with parachute size inhibited direct comparison of C_m values from this investigation with past work.

Appendix

A. Calculating the Total Angle of Attack

For ease of explanation, the current discussion assumes that motion is restricted to the pitch plane, although the theory is applied similarly to motion in the yaw plane. Canopy rotation about the ball joint in the pitch plane is shown in Figs. 17a and 17b. Rotation of the canopy results in a velocity component that is tangent to the canopy's circular arc of motion (V_t). Aerodynamic forces act through the center of pressure of the parachute, which is generally located near the skirt of the canopy (R_{cp}). Since the canopy forces are computed with respect to the total angle of attack and the velocity of the canopy, the velocity and total angle of attack are calculated at the center of pressure. The tangential velocity is given in Eq. 17. The velocity V_c is the wind velocity at the canopy, which is assumed to act along the tunnel centerline and have a larger magnitude than the freestream wind velocity due to blockage effects. The resulting velocity triangles seen in Figs. 17c and 17d give rise to the actual wind velocity (V_w) at the center of pressure of the canopy and a dynamic angular component of the angle of attack. Note that the sign of the pitch rate ($\dot{\theta}$) depends on whether the canopy is rotating away from the tunnel centerline (positive) or towards the centerline (negative). Additionally, note that the direction of the tangential velocity in Figs. 17c and 17d is equal and opposite of that shown in Figs. 17a and 17b because the wind velocity with respect to the canopy is equal and opposite of the velocity of the canopy with respect to the wind.
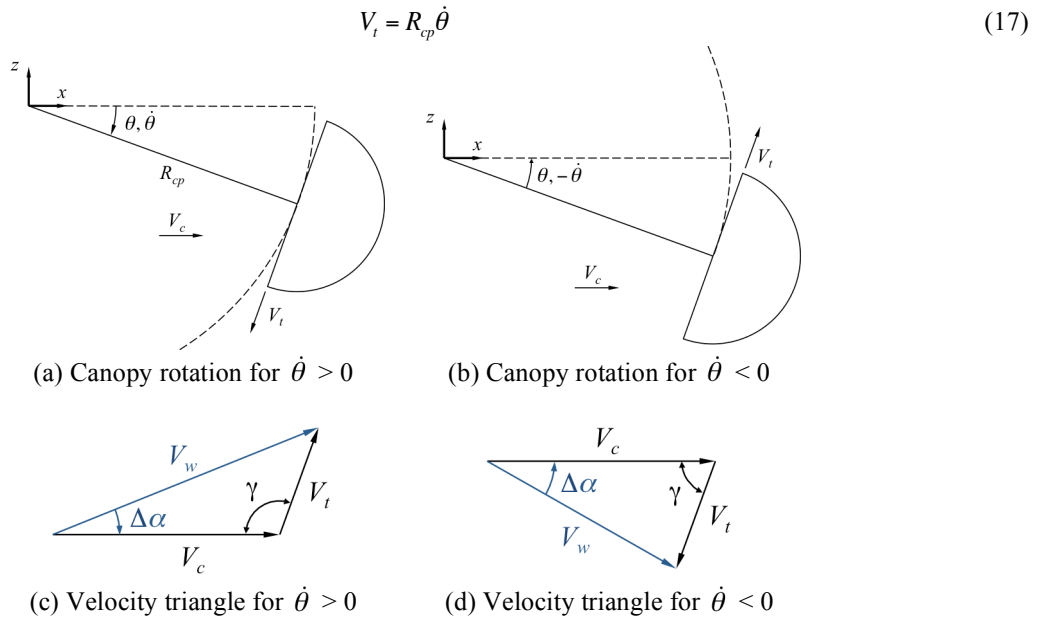
$$V_t = R_{cp}\dot{\theta} \tag{17}$$

(a) Canopy rotation for $\dot{\theta} > 0$ (b) Canopy rotation for $\dot{\theta} < 0$

(c) Velocity triangle for $\dot{\theta} > 0$ (d) Velocity triangle for $\dot{\theta} < 0$

Figure 17. Diagram of canopy rotation and the resulting wind velocity triangle for motion in the pitch plane.

The angle γ is defined as the angle between V_c and V_t and is given in Eq. (18). In Eq. (18), "sgn" is the sign of the function and is equal to +1 when the pitch rate is positive and -1 when the pitch rate is negative. The actual wind velocity V_w is then calculated via the Law of Cosines as in Eq. (19).

$$\gamma = \frac{\pi}{2} + \mathbf{sgn}\left(\dot{\theta}\right)\theta \tag{18}$$

$$V_w^2 = V_c^2 + V_t^2 - 2V_cV_t\cos\gamma \tag{19.1}$$

$$V_w = \sqrt{V_c^2 + R_{cp}^2\dot{\theta}^2 - 2V_c\left|R_{cp}\dot{\theta}\right|\cos\left[\frac{\pi}{2} + \text{sign}\left(\dot{\theta}\right)\theta\right]} \tag{19.2}$$

With V_w, V_t, and γ known, the dynamic angle of attack correction $\Delta\alpha$ can be calculated via the Law of Sines as in Eq. (20). The angle of attack is then the sum of the geometric pitch angle and the dynamic correction, as in Eq. (21).

$$\frac{\sin\Delta\alpha}{V_{t_\theta}} = \frac{\sin\gamma_\theta}{V_{w_\theta}} \tag{20.1}$$

$$\Delta\alpha = \sin^{-1}\left[\frac{\left|R_{cp}\dot\theta\right|}{\sqrt{V_c^2 + R_{cp}^2\dot\theta^2 - 2V_c\left|R_{cp}\dot\theta\right|\cos\left[\frac{\pi}{2} + \mathrm{sgn}\left(\dot\theta\right)\theta\right]}}\sin\left[\frac{\pi}{2} + \mathrm{sgn}\left(\dot\theta\right)\theta\right]\right] \tag{20.2}$$

$$\alpha = \theta + \Delta\alpha \tag{21}$$

Angle correction in the yaw plane is similar to the correction in the pitch plane. Therefore, the aerodynamic sideslip angle and its dynamic correction are given Eq. (22).

$$\Delta\beta = \sin^{-1}\left[\frac{\left|R_{cp}\dot\psi\right|}{\sqrt{V_c^2 + R_{cp}^2\dot\psi^2 - 2V_c\left|R_{cp}\dot\psi\right|\cos\left[\frac{\pi}{2} + \mathrm{sgn}\left(\dot\psi\right)\psi\right]}}\sin\left[\frac{\pi}{2} + \mathrm{sgn}\left(\dot\psi\right)\psi\right]\right] \tag{22.1}$$

$$\beta = \psi + \Delta\beta \tag{22.2}$$

The total angle of attack, accounting for both static and dynamic contributions, is given in Eq. (23). Note that the total angle of attack is always positive due to its physical definition.

$$\cos\alpha_T = \cos\alpha\cos\beta \tag{23.1}$$

$$\alpha_T = \cos^{-1}\left[\cos\alpha\cos\beta\right] \tag{23.2}$$

B. Calculating Derivatives of the Total Angle of Attack

The derivative of the total angle of attack can be calculated by taking the derivative of Eq. (23.1).

$$\dot\alpha_T = \frac{\dot\alpha\sin\alpha\cos\beta + \dot\beta\cos\alpha\sin\beta}{\sin\alpha_T} \tag{24}$$

The derivative of the angle of attack and the sideslip angle are equal to the sum of the derivatives of the static and dynamic components, as in Eq. (25). Derivatives of the dynamic contributions are given in Eq. (26).

$$\dot\alpha = \dot\theta + \Delta\dot\alpha \tag{25.1}$$

$$\dot\beta = \dot\psi + \Delta\dot\beta \tag{25.2}$$

$$\Delta\dot\alpha = \frac{\dot V_{t_\theta}V_{w_\theta} - V_{t_\theta}\dot V_{w_\theta}}{V_{w_\theta}^2}\frac{\sin\gamma_\theta}{\cos\Delta\alpha} + \frac{V_{t_\theta}}{V_{w_\theta}}\frac{\cos\gamma_\theta}{\cos\Delta\alpha}\dot\gamma_\theta \tag{26.1}$$

$$\Delta\dot\beta = \frac{\dot V_{t_\psi}V_{w_\psi} - V_{t_\psi}\dot V_{w_\psi}}{V_{w_\psi}^2}\frac{\sin\gamma_\psi}{\cos\Delta\beta} + \frac{V_{t_\psi}}{V_{w_\psi}}\frac{\cos\gamma_\psi}{\cos\Delta\beta}\dot\gamma_\psi \tag{26.2}$$

The derivatives of the tangential canopy velocity in the pitch plane ($\dot\gamma_\theta$) and the actual wind velocity in the pitch plane can be found by differentiating Eqs. (17), (18) and (19.1) and are calculated via Eqs. (27.1.1), (27.1.2), and (27.1.3) respectively. The derivatives of the tangential canopy velocity in the yaw plane ($\dot\gamma_\psi$) and the actual wind

velocity in the yaw plane can be found in the same way and are calculated via Eqs. (27.2.1), (27.2.2), and (27.2.3) respectively.

$$\dot{V}_{t_\theta} = R_{cp}\ddot{\theta} \tag{27.1.1}$$

$$\dot{\gamma}_\theta = \dot{\theta} \tag{27.1.2}$$

$$\dot{V}_{w_\theta} = \frac{\dot{V}_{t_\theta}\left(V_{t_\theta} - V_c\cos\gamma_\theta\right) + \dot{\gamma}_\theta V_c V_{t_\theta}\sin\gamma_\theta}{V_{w_\theta}} \tag{27.1.3}$$

$$\dot{V}_{t_\psi} = R_{cp}\ddot{\theta} \tag{27.2.1}$$

$$\dot{\gamma}_\psi = \dot{\psi} \tag{27.2.2}$$

$$\dot{V}_{w_\psi} = \frac{\dot{V}_{t_\psi}\left(V_{t_\psi} - V_c\cos\gamma_\psi\right) + \dot{\gamma}_\psi V_c V_{t_\psi}\sin\gamma_\psi}{V_{w_\psi}} \tag{27.2.3}$$

The second derivative of the total angle of attack can be calculated by twice differentiating Eq. (23.1). The remaining derivation proceeds in the same fashion as for the first derivative (given in Eqs. (24) through (27)).

$$\ddot{\alpha}_T = \frac{\ddot{\alpha}\sin\alpha\cos\beta + \ddot{\beta}\cos\alpha\sin\beta + \left(\dot{\alpha}^2 + \dot{\beta}^2 - \dot{\alpha}_T^2\right)\cos\alpha_T - 2\dot{\alpha}\dot{\beta}\sin\alpha\sin\beta}{\sin\alpha_T} \tag{28}$$

$$\ddot{\alpha} = \ddot{\theta} + \Delta\ddot{\alpha} \tag{29.1}$$

$$\ddot{\beta} = \ddot{\psi} + \Delta\ddot{\beta} \tag{29.2}$$

$$\Delta\ddot{\alpha} = \frac{1}{\cos\Delta\alpha}\left[\begin{array}{l}\dfrac{\left(\ddot{V}_{t_\theta}V_{w_\theta} - V_{t_\theta}\ddot{V}_{w_\theta}\right)\left(V_{w_\theta}^2\right) - \left(\dot{V}_{t_\theta}V_{w_\theta} - V_{t_\theta}\dot{V}_{w_\theta}\right)\left(2V_{w_\theta}\dot{V}_{w_\theta}\right)}{V_{w_\theta}^4}\sin\gamma_\theta + \\[2ex] 2\dfrac{\dot{V}_{t_\theta}V_{w_\theta} - V_{t_\theta}\dot{V}_{w_\theta}}{V_{w_\theta}^2}\dot{\gamma}_\theta\cos\gamma_\theta + \dfrac{V_{t_\theta}}{V_{w_\theta}}\left(\dot{\gamma}_\theta^2\sin\gamma_\theta + \ddot{\gamma}_\theta\cos\gamma_\theta\right) + \Delta\dot{\alpha}^2\sin\Delta\alpha\end{array}\right] \tag{30.1}$$

$$\Delta\ddot{\beta} = \frac{1}{\cos\Delta\beta}\left[\begin{array}{l}\dfrac{\left(\ddot{V}_{t_\psi}V_{w_\psi} - V_{t_\psi}\ddot{V}_{w_\psi}\right)\left(V_{w_\psi}^2\right) - \left(\dot{V}_{t_\psi}V_{w_\psi} - V_{t_\psi}\dot{V}_{w_\psi}\right)\left(2V_{w_\psi}\dot{V}_{w_\psi}\right)}{V_{w_\psi}^4}\sin\gamma_\psi + \\[2ex] 2\dfrac{\dot{V}_{t_\psi}V_{w_\psi} - V_{t_\psi}\dot{V}_{w_\psi}}{V_{w_\psi}^2}\dot{\gamma}_\psi\cos\gamma_\psi + \dfrac{V_{t_\psi}}{V_{w_\psi}}\left(\dot{\gamma}_\psi^2\sin\gamma_\psi + \ddot{\gamma}_\psi\cos\gamma_\psi\right) + \Delta\dot{\beta}^2\sin\Delta\beta\end{array}\right] \tag{30.2}$$

$$\ddot{V}_{t_\theta} = R_{cp}\dddot{\theta} \tag{31.1.1}$$

$$\ddot{\gamma}_\theta = \ddot{\theta} \tag{31.1.2}$$

$$\ddot{V}_{w_\theta} = \frac{1}{V_{w_\theta}}\left[\dot{V}_{t_\theta}^2 + \ddot{V}_{t_\theta}\left(V_{t_\theta} - V_c\cos\gamma_\theta\right) + 2\dot{\gamma}_\theta V_c\dot{V}_{t_\theta}\sin\gamma_\theta + V_c V_{t_\theta}\left(\ddot{\gamma}_\theta\sin\gamma_\theta + \dot{\gamma}_\theta^2\cos\gamma_\theta\right) - \dot{V}_{w_\theta}^2\right] \tag{31.1.3}$$

$$\ddot{V}_{t_\psi} = R_{cp}\dddot{\psi} \tag{31.2.1}$$

$$\ddot{\gamma}_\psi = \ddot{\psi} \tag{31.2.2}$$

$$\ddot{V}_{w_\psi} = \frac{1}{V_{w_\psi}}\left[\dot{V}_{t_\psi}^2 + \ddot{V}_{t_\psi}\left(V_{t_\psi} - V_c\cos\gamma_\psi\right) + 2\dot{\gamma}_\psi V_c\dot{V}_{t_\psi}\sin\gamma_\psi + V_c V_{t_\psi}\left(\ddot{\gamma}_\psi\sin\gamma_\psi + \dot{\gamma}_\psi^2\cos\gamma_\psi\right) - \dot{V}_{w_\psi}^2\right] \tag{31.2.3}$$

C. Local Wind Velocity at the Canopy

The parachute center of pressure can be expressed in the inertial frame via the transformation matrix in Eq. (1). The inertial coordinates of the center of pressure are found in Eq. (32).

$$\mathbf{R}_{cp} = R_{cp} \begin{bmatrix} \cos\theta\cos\psi \\ \sin\psi \\ -\sin\theta\cos\psi \end{bmatrix} \tag{32}$$

The inertial angular velocity vector ($\mathbf{\Omega}$) of the canopy can be determined by rotating the Euler angle rates back to the inertial frame, as in Eq. (33).

$$\mathbf{\Omega} = \begin{bmatrix} \cos\theta & 0 & \sin\theta \\ 0 & 1 & 0 \\ -\sin\theta & 0 & \cos\theta \end{bmatrix} \begin{bmatrix} 0 \\ \dot{\theta} \\ 0 \end{bmatrix} + \begin{bmatrix} \cos\theta & 0 & \sin\theta \\ 0 & 1 & 0 \\ -\sin\theta & 0 & \cos\theta \end{bmatrix} \begin{bmatrix} \cos\psi & -\sin\psi & 0 \\ \sin\psi & \cos\psi & 0 \\ 0 & 0 & 1 \end{bmatrix} \begin{bmatrix} 0 \\ 0 \\ \dot{\psi} \end{bmatrix} \tag{33.1}$$

$$\mathbf{\Omega} = \begin{bmatrix} \dot{\psi}\sin\theta \\ \dot{\theta} \\ \dot{\psi}\cos\theta \end{bmatrix} \tag{33.2}$$

Knowing the inertial coordinates of the parachute center of pressure and the inertial angular velocity, the tangential velocity vector ($\mathbf{V_t}$) of the canopy can be determined via Eq. (34).

$$\mathbf{V}_t = \mathbf{\Omega} \times \mathbf{R}_{cp} \tag{34.1}$$

$$\mathbf{V_t} = \begin{bmatrix} \dot{x}_{cp} \\ \dot{y}_{cp} \\ \dot{z}_{cp} \end{bmatrix} = R_{cp} \begin{bmatrix} -\dot{\theta}\sin\theta\cos\psi - \dot{\psi}\cos\theta\sin\psi \\ \dot{\psi}\cos\psi \\ -\dot{\theta}\cos\theta\cos\psi + \dot{\psi}\sin\theta\sin\psi \end{bmatrix} \tag{34.2}$$

The total wind velocity at the canopy is the sum of the blockage-corrected wind velocity and the wind velocity due to tangential motion of the canopy. The actual wind velocity vector and magnitude are given in Eq. (35).

$$\mathbf{V}_w = \begin{bmatrix} V_c \\ 0 \\ 0 \end{bmatrix} - \begin{bmatrix} \dot{x}_{cp} \\ \dot{y}_{cp} \\ \dot{z}_{cp} \end{bmatrix} = \begin{bmatrix} V_c + R_{cp}(\dot{\theta}\sin\theta\cos\psi + \dot{\psi}\cos\theta\sin\psi) \\ -R_{cp}\dot{\psi}\cos\psi \\ R_{cp}(\dot{\theta}\cos\theta\cos\psi - \dot{\psi}\sin\theta\sin\psi) \end{bmatrix} \tag{35.1}$$

$$V_w = \sqrt{\left(V_c - \dot{x}_{cp}\right)^2 + \dot{y}_{cp}^2 + \dot{z}_{cp}^2} \tag{35.2}$$

Acknowledgments

References

[1] J. R. Cruz and J. S. Lingard, "Aerodynamic Decelerators for Planetary Exploration: Past, Present, and Future," *AIAA Guidance, Navigation, and Control Conference and Exhibit*, p. 20, Aug. 2006.

[2] Maynard, J. D., "Aerodynamic Characteristics of Parachutes at Mach Numbers from 1.6 to 3," NASA TN D-752, 1961.

[3] Charczenko, N., "Wind-Tunnel Investigation of Drag and Stability of Parachutes at Supersonic Speeds," NASA TM X-991, 1964.

[4] Mayhue, R. J. and Bobbitt, P. J., "Drag Characteristics of a Disk-Gap-Band Parachute with a Nominal Diameter of 1.65 Meters at Mach Numbers from 2.0 to 3.0," NASA TN D 6894, 1972

[5] Lundstrom, R. R., Darnell, W. L., and Henning, A. B., "A Method for Making Large-Scale Decelerator Tests in a Simulated Mars Environment," AIAA Paper 68-241, 1968.

[6] McFall, J. C. and Murrow Jr., H. N., "Parachute Testing at Altitudes Between 30 and 90 Kilometers," Journal of Spacecraft and Rockets, Vol. 4, June, 1967, pp. 796-798.

[7] Eckstrom, C. V. and Murrow, H. N., "Flight Test of a 40-Foot-Nominal-Diameter Modified Ringsail Parachute Deployed at a Mach Number of 1.64 and a Dynamic Pressure of 9.1 Pounds per Square Foot," NASA TM X-1484, 1967.

[8] Eckstrom, C. V. and Preisser, J. S., "Flight Test of a 30-Foot-Nominal-Diameter Disk Gap-Band Parachute Deployed at a Mach Number of 1.56 and a Dynamic Pressure of 11.4 Pounds per Square Foot," NASA TM X-1451, 1967.

[9] Darnell, W. L., Henning, A. B., and Lundstrom, R. R., "Flight Test of a 15-Foot Diameter (4.6 Meter) 120° Conical Spacecraft Simulating Parachute Deployment in a Mars Atmosphere," NASA TN D-4266, 1967.

[10] Preisser, J. S. and Eckstrom, C. V., "Flight Test of a 31.2-Foot-Diameter Modified Ringsail Parachute Deployed at a Mach Number of 1.39 and a Dynamic Pressure of 11.0 Pounds per Square Foot," NASA TM X-1414, 1967.

[11] Whitlock, C. H., Bendura, R. J., and Coltrane, L. C., "Performance of a 26-Meter Diameter Ringsail Parachute in a Simulated Martian Environment," NASA TM X-1356, 1967.

[12] Bendura, R. J., Huckins III, E. K., and Coltrane, L. C., "Performance of a 19.7-Meter Diameter Disk-Gap-Band Parachute in a Simulated Martian Environment," NASA TM X 1499, 1968.

[13] Eckstrom, C. V. and Preisser, J. S., "Flight Test of a 40-Foot-Nominal-Diameter Disk Gap-Band Parachute Deployed at a Mach Number of 2.72 and a Dynamic Pressure of 9.7 Pounds per Square Foot," NASA TM X-1623, 1968.

[14] Lundstrom, R. R., Darnell, W. L., and Coltrane, L. C., "Performance of a 16.6-Meter Diameter Cross Parachute in a Simulated Martian Environment," NASA TM X-1543, 1968.

[15] Preisser, J. S. and Eckstrom, C. V., "Flight Test of a 30-Foot-Nominal-Diameter Cross Parachute Deployed at a Mach Number of 1.57 and a Dynamic Pressure of 9.7 Pounds per Square Foot," NASA TM X-1542, 1968.

[16] Preisser, J. S. and Eckstrom, C. V., "Flight Test of a 40-Foot-Nominal-Diameter Disk Gap-Band Parachute Deployed at a Mach Number of 1.91 and a Dynamic Pressure of 11.6 Pounds per Square Foot," NASA TM X-1575, 1968.

[17] Whitlock, C. H., Henning, A. B., and Coltrane, L. C., "Performance of a 16.6-Meter Diameter Modified Ringsail Parachute in a Simulated Martian Environment," NASA TM X-1500, 1968.

[18] Eckstrom, C. V., "High-Altitude Flight Test of a 40-Foot-Diameter (12.2-meter) Ringsail Parachute at a Deployment Mach Number of 2.95," NASA TN D-5796, 1970.

[19] Eckstrom, C. V., "Flight Test of a 40-Foot-Nominal-Diameter Disk-Gap-Band Parachute Deployed at a Mach Number of 3.31 and a Dynamic Pressure of 10.6 Pounds per Square Foot," NASA TM X-1924, 1970.

[20] Preisser, J. S. and Grow, R. B., "High-Altitude Flight Test of a Reefed 12.2-Meter Diameter Disk-Gap-Band Parachute with Deployment at a Mach Number of 2.58," NASA TN D-6469, 1971.

[21] Eckstrom, C. V. and Branscome, D. R., "High-Altitude Flight Test of a Disk-Gap-Band Parachute Deployed Behind a Bluff Body at a Mach Number of 2.69," NASA TM X-2671, 1972.

[22] Murrow, H. N. and McFall Jr., J. C., "Some Test Results from the NASA Planetary Entry Parachute Program," Journal of Spacecraft and Rockets, Vol. 6, No. 5, 1969, pp. 621-623.

[23] H. N. Murrow and C. V. Eckstrom, "Low- and High-Altitude Tests of Parachutes Designed for Use in Low Density Atmospheres," presented at the AIAA Aerodynamic Deceleration Systems Conference, Dayton, OH, 1970, p. 6.

[24] H. N. Murrow and C. V. Eckstrom, "Performance of Disk-Gap-Band, Ringsail, and Cross Parachutes at Low Earth Altitude," Journal of Spacecraft, vol. 8, no. 4, pp. 418–420, Apr. 1971.

[25] H. N. Murrow and J. C. McFall Jr, "Summary of Experimental Results Obtained From the NASA Planetary Entry Parachute Program," presented at the Aerodynamic Deceleration Systems Conference, El Centro, CA, 1968, p. 7.

[26] S. Steinberg, P. Siemers III, and R. Slayman, "Development of the Viking Parachute Configuration by Wind-Tunnel Investigation," Journal of Spacecraft and Rockets, vol. 11, no. 2, pp. 101–107, Feb. 1974.

[27] H. N. Murrow, C. V. Eckstrom, and D. W. Henke, "Development Flight Tests of the Viking Decelerator System," presented at the AIAA Aerodynamic Decelerator Systems Conference, Palm Spring, CA, 1973, p. 8.

[28] Moog, R. D., Bendura, R. J., Timmons, J. D., and Lau, R. A., "Qualification Tests of the Viking Decelerator System," Journal of Spacecraft and Rockets, Vol. 11, No. 3, 1974, pp. 188-195.

[29] Fallon, E. J., "System Design Overview of the Mars Pathfinder Parachute Decelerator Subsystem." AIAA, (97-1511), 1997.

[30] Steltzner, A., Cruz, J., Bruno, R., and Mitcheltree, R., "Opportunities and Limitations in Low Earth Subsonic Testing for Qualification of Extraterrestrial Supersonic Parachute Designs," AIAA Paper 2003-2135, 2003.

[31] Taeger, Y. and Witkowski, A., "A Summary of Dynamic Testing of the Mars Exploration Rover Parachute Decelerator System," AIAA Paper 2003-2127, 2003.

[32] Way, D. W., Desai, P. N., Engelund, W. C., Cruz, J. R., and Hughes, S. J., "Design and Analysis of the Drop Test Vehicle for the Mars Exploration Rover Parachute Structural Tests," AIAA Paper 2003-2128, 2003.

[33] Cruz, J. R., Kandis, M., and Witkowski, A., "Opening Loads Analyses for Various Disk-Gap-Band Parachutes," AIAA Paper 2003-2131, 2003.

[34] Zell, P. T., Cruz, J. R., and Witkowski, A., "Structural Testing of Parachutes in the National Full-Scale Aerodynamics Complex 80-by-120-foot Wind Tunnel at NASA Ames Research Center," AIAA Paper 2003-2130, 2003.

[35] Cruz, J. R., Mineck, R. E., Keller, D. F., and Bobskill, M. V., "Wind Tunnel Testing of Various Disk-Gap-Band Parachutes," AIAA Paper 2003-2129, 2003.

[36] A. Witkowski, W. Machalick, and Y. Taeger, "Mars Subsonic Parachute Technology Task System Overview," presented at the AIAA Aerodynamic Decelerator Systems Technology Conference and Seminar, Munich, Germany, 2005, p. 9.

[37] R. A. Mitcheltree, R. Bruno, E. Slimko, C. Baffes, E. Konefat, and A. Witkowski, "High Altitude Test Program For A Mars Subsonic Parachute," presented at the AIAA Aerodynamic Decelerator Systems Technology Conference and Seminar, Munich, Germany, 2005, p. 11.

[38] Raiszadeh, B., Kandis, M., Cruz, J. R., Bailey, E. S., Mineck, R. E., ``Performance Analysis of a 33.5 m Diameter Ringsail Parachute at Low- and High-Altitudes,'' AIAA Paper 2005-1658, May, 2005.

[39] Adams D.S., Witkowski A. and Kandis M. "Phoenix Mars Scout Parachute Flight Behavior and Observations", IEEE Aerospace Conference, IEEEAC 1534, January 2011.

[40] Adams, D. S., and Rivellini, T. P., "Mars Science Laboratory's Parachute Qualification Approach," AIAA Paper 2009-2913, 2009.

[41] Witkowski, A., Kandis, M., and Adams, D. S., "Inflation Characteristics of the MSL Disk Gap Band Parachute," 20th AIAA Aerodynamic Decelerator Systems Technology Conference and Seminar, Seattle, WA, May 4-7, 2009, AIAA-2009-2915.

[42] Witkowski, A., Kandis, M., Sengupta, A., and Long, K. "Comparison of Subscale Versus Full Scale Wind Tunnel Tests of MSL Disk Gap Band Parachutes," presented at the AIAA Aerodynamic Decelerator Systems Technology Conference and Seminar, Seattle, WA, 2009, p. 6.

[43] Sengupta, A., et al., "Results from the Mars Science Laboratory Parachute Decelerator System Supersonic Qualification Program," 2008 IEEE Aerospace Conference, March 1-8, Big Sky, MT, IEEEAC-1435.

[44] Sengupta, A., Kelsch, R., Roeder, J., Wernet, M., Witkowski, A., and Kandis, M. "Supersonic Performance of Disk-Gap-Band Parachutes Constrained to a 0-Degree Trim Angle," *Journal of Spacecraft and Rockets*, vol. 46, no. 6, pp. 1155–1163, Nov. 2009.

[45] Sengupta, A., Steltzner, A., Witkowski, A., Candler, G. V., and Pantano, C. "Findings From the Supersonic Qualification Program of the Mars Science Laboratory Parachute System," presented at the AIAA Aerodynamic Decelerator Systems Technology Conference and Seminar, Seattle, WA, 2009, p. 16.

[46] Sengupta, A. Steltzner, A., Comeaux, K., Candler, G. V., Pantano, C., and Bell, J. "Supersonic Delta Qualification by Analysis Program for the Mars Science Laboratory Parachute Decelerator System," presented at the AIAA Aerodynamic Decelerator Systems Technology Conference and Seminar, Williamsburg, VA, 2007, p. 17.

[47] V. Gidzak et. al., "Simulation of Fluid-Structure Interaction of the Mars Science Laboratory Parachute," AIAA 2008-6910, August 2008.

[48] M. Barnhardt, T. Drayna, Ioannis Nompelis, G.V. Candler, and W. Garrard, "Detached Eddy Simulations of the MSL Parachute at Supersonic Conditions," AIAA-2529-2007, May 2007.

[49] Gallon, J. C., Clark, I. G., Rivellini, T. P., Adams, D. S., and Witkowski, A., "Low Density Supersonic Decelerator Parachute Decelerator System," AIAA Aerodynamic Decelerator Systems Technology Conference and Seminar, March 2013.

[50] Schoenenberger, M., Queen, E. M., and Cruz, J. R., "Parachute Aerodynamics from Video Data," AIAA Aerodynamic Decelerator Systems Technology Conference and Seminar, AIAA 2005-1633, May 2005.

[51] Tanner, C., Clark, I., Gallon, J., Rivellini, T., and Witkowski, A., "Aerodynamic Characterization of New Parachute Configurations for Low-Density Deceleration," 22nd AIAA Aerodynamic Decelerator Systems Conference, Daytona Beach, CA, March 2013.

[52] Kushner, L.K. and Schairer, E.T., "Planning Image-Based Measurements in Wind Tunnels by Virtual Imaging," AIAA Paper 2011-0930, presented at 49th AIAA Aerospace Sciences Meeting and Exhibit, Orlando, FL, Jan. 2011.

[53] Abdel-Aziz, Y.I. and Karara, H.M., "Direct Linear Transformation from comparator coordinates into object-space coordinates," Proceedings, Symposium on Close-Range Photogrammetry, American Society of Photogrammetry, Urbana, IL, Jan. 1971.

[54] McBride, D. D., "Orbiter Drag Chute Stability Test in the NASA Ames 80x120 Foot Wind Tunnel," Tech. Rep. SAND-93-2544, Sandia National Laboratories, Albuquerque, NM, Feb. 1994.

[55] Cockrell, D., Doherr, K. F., "Preliminary Consideration of Parameter Identification Analysis from Parachute Aerodynamic Flight Test Data," AIAA Paper 1981-1940, AIAA Aerodynamic Decelerator and Balloon Technology Conference, Oct. 1981.

[56] Ibrahim, S. K., "Experimental Determination of the Apparent Moment of Inertia of Parachutes," Tech. Rep. AFFDL-TDR-64-153, Air Force Flight Dynamics Laboratory, Wright-Patterson Air Force Base, Ohio, April 1965.